Altair-LSFM: A High-Resolution, Easy-to-Build Light-Sheet Microscope for Sub-Cellular Imaging.

John Haug[1,2], Seweryn Gałecki[1,2,3], and Kevin M. Dean[1,2]

Affiliations:

[1] *Lyda Hill Department of Bioinformatics, UT Southwestern Medical Center, Dallas, TX 75390, USA.*

[2] *Cecil H. and Ida Green Center for Systems Biology, UT Southwestern Medical Center, Dallas, TX 75390, USA.*

[3] *Department of Systems Biology and Engineering, Silesian University of Technology, Akademicka 16, 44-100 Gliwice, Poland.*

Correspondence:

kevin.dean@utsouthwestern.edu

Abstract: Although several open-source, easy-to-assemble light-sheet microscope platforms already exist—such as mesoSPIM, OpenSPIM, and OpenSpin—they are primarily optimized for imaging large specimens and lack the resolution required to visualize sub-cellular organelles or cytoskeletal architectures. Conversely, commercial systems like Lattice Light-Sheet Microscopy offer improved resolution but are complex, expensive, and alignment-intensive. To address this gap, we developed Altair-LSFM, a high-resolution, open-source, sample-scanning light-sheet microscope specifically designed for sub-cellular imaging. By optimizing the optical pathway in silico, we created a custom baseplate with precisely positioned dowel pins to simplify alignment and assembly. The system integrates streamlined optoelectronics and optomechanics with seamless operation through our open-source software, navigate. Altair-LSFM achieves lateral and axial resolutions of approximately 235 nm and 350 nm, respectively, across a 266-micron field of view after deconvolution. We validate the system's capabilities by imaging sub-diffraction fluorescent nanospheres and visualizing fine structural details in mammalian cells, including microtubules, actin filaments, nuclei, and Golgi apparatus.

Introduction: Light-sheet fluorescence microscopy (LSFM) has revolutionized volumetric imaging by enabling rapid, minimally invasive 3D investigations of diverse biological specimens[1]. By illuminating the sample with a thin sheet of light from the side and capturing 2D images in a highly parallel format, LSFM dramatically reduces photobleaching and out-of-focus blur. Interestingly, the first concept of LSFM was documented as early as 1903, and nearly nine decades later, it was adapted to visualize cochlear structures[2]. However, LSFM truly entered the limelight in 2004[1], sparking the development of numerous specialized variants—each suited to unique biological tasks. Collectively, these methods have facilitated the long-term tracking of cells through embryological development[3], the mapping of brain architecture[4] and activation patterns[5], and much more, making LSFM indispensable for a wide array of dynamic, 3D imaging applications.

While these milestones highlight LSFM's transformative potential, it wasn't until the early 2010s that researchers harnessed LSFM for sub-cellular imaging[6]. Achieving this level of detail demands optimizing both resolution and sensitivity, which are fundamentally dictated by the numerical aperture (NA) of the microscope's objectives. More specifically, lateral resolution is governed by the fluorophore's emission wavelength and the NA of the detection objective, while photon collection efficiency scales with the detection objective's NA^2, making high-NA objectives essential for resolving fine, less abundantly labeled structures, while maximizing signal. Axial resolution, in turn, is set by the detection objective's depth of focus and the thickness of the illumination beam. When the illumination beam is thinner than the depth of focus, it's thickness essentially becomes the axial resolution[7]. Conversely, if the illumination beam is larger than the depth of focus, then the depth of focus takes precedence, and fluorescence elicited outside this region contributes to the image as blur. Importantly, there is a trade-off between

field of view, axial resolution, and NA: pushing for high axial resolution often constrains the accessible field of view, necessitating careful mechanical and optical design choices.

Bounded by these fundamental constraints, several methods have been developed to achieve sub-cellular resolution in LSFM. For example, one can illuminate the specimen with a propagation-invariant beam[6] or an optical lattice[8]. This can be done coherently, as in Lattice Light-Sheet Microscopy (LLSM)[8], or incoherently, as in Field Synthesis[9]. However, the most used optical lattice, the four-beam "square" lattice, offers little advantage over a traditional Gaussian beam[10]. Another approach, dual view inverted Selective Plane Illumination Microscopy (diSPIM), captures images from multiple orthogonal perspectives and computationally fuses them using iterative deconvolution, significantly improving axial resolution[11]. However, this method requires precise image registration and intensive computational processing. Axially Swept Light-sheet Microscopy (ASLM)[12] extends the field of view while maintaining high axial resolution but operates at lower speeds and sensitivity compared to LLSM and diSPIM, making it less suitable for fast volumetric imaging. Oblique plane microscopy (OPM) offers another alternative by imaging an obliquely launched light sheet with a non-coaxial and complex optical train, allowing for single-objective light-sheet imaging but introducing substantial alignment challenges[13]. While these techniques offer powerful solutions for sub-cellular imaging, they all require expert assembly and precise optical alignment, limiting their widespread adoption. As a result, there remains a critical need for a high-resolution, accessible LSFM system that combines cutting-edge imaging performance with ease of assembly and operation.

To address these limitations, we developed Altair-LSFM, a high-resolution, open-source light-sheet microscope that achieves sub-cellular detail while remaining accessible and easy to use. Named after the navigational star, Altair-LSFM is built upon two guiding optical principles. First, in LLSM, the sole improvement in lateral resolution comes from the use of a higher-NA detection objective, which we incorporate to maximize both resolution and photon collection efficiency. Second, when diffraction effects are fully accounted for, a tightly focused Gaussian beam achieves a beam waist and propagation length that is comparable to that of a square lattice, eliminating the need for specialized optical components while preserving high axial resolution. By leveraging these principles, Altair-LSFM delivers optical performance on par with LLSM but without the added design complexity of LLSM. To streamline assembly and ensure reproducibility, we designed the optical layout for Altair-LSFM in silico, enabling a pre-defined optical alignment with minimal degrees of freedom. A custom-machined baseplate with precisely positioned dowel pins locks optical components into place, minimizing degrees of freedom and removing the need for fine manual adjustments. Additionally, by simplifying the optomechanical design and integrating compact optoelectronics, Altair-LSFM reduces system complexity, making advanced light-sheet imaging more practical for a wider range of laboratories.

By combining high-resolution imaging with an accessible and reproducible design, Altair-LSFM addresses a critical gap in LSFM—bringing sub-cellular imaging capabilities to a broader scientific community. Its reliance on fundamental microscopy principles rather than overly complex optical systems ensures both performance and simplicity, while its modular architecture allows for straightforward assembly and operation. By eliminating the need for specialized optics and intricate alignment procedures, Altair-LSFM significantly lowers the barrier to adoption, making advanced light-sheet imaging feasible for laboratories that lack the resources or expertise to implement more complex systems. This combination of performance, accessibility, and scalability establishes Altair-LSFM as a powerful and practical solution for a wide range of laboratories.

Results

Survey of Open-Source LSFM Designs. Before designing Altair-LSFM, we first evaluated existing open-source LSFM implementations to identify common design features, constraints, and trade-offs (**Table 1**). Many systems, such as UC2[14], pLSM[15], and EduSPIM[16], were explicitly developed with cost-effectiveness in mind, relying on low-cost components and simplified designs to maximize accessibility. Others, including OpenSPIM[17,18], OpenSPIN[19], and mesoSPIM[20,21], were optimized for imaging large specimens, such as developing embryos or chemically cleared tissues. Most of these systems employed modular construction methods based on rail carriers or cage systems, which,

while reducing alignment complexity compared to free-space optics, still retain degrees of freedom that can lead to misalignment and increase setup difficulty. As a result, these microscopes generally operate at low magnification and low NA, limiting their ability to resolve sub-cellular structures. Among the surveyed designs, only diSPIM[11,22] was explicitly developed for sub-cellular imaging, built with a dovetail-based system for precise optical alignment. However, diSPIM's most widely deployed configuration uses NA 0.8 objectives, which limits its photon collection efficiency and resolution. Consequently, the cell biology community lacks an open-source light-sheet microscope that combines state-of-the-art resolution with ease of assembly, robust optical alignment, and streamlined computational processing.

Design Principles of Altair-LSFM.

Building on these findings, we designed Altair-LSFM to achieve performance comparable to LLSM[8] while maintaining a compact footprint and streamlined assembly. While cost-effectiveness was considered in the design process, the inclusion of high-NA optics and performant, low-noise cameras inherently increase system cost. To simplify procurement and integration, we minimized the number of required manufacturers while maintaining high-performance components. Excluding the laser source-which varies significantly in price depending upon the number of lasers, power, and modulation requirements, the estimated price for Altair-LSFM is $150,000. A detailed list of all system components, their sources, and associated costs is provided in **Supplementary Tables S2 and S3**.

Altair-LSFM is configured to operate in a sample-scanning format with a detection path that is nearly identical to that of LLSM, ensuring similar lateral resolution (~230 nm × 230 nm × 370 nm) and photon collection efficiency. Specifically, we paired a 25x NA 1.1 water-dipping physiology objective (Nikon N25X-APO-MP) with a 400 mm achromatic tube lens (Applied Scientific Instrumentation), ensuring Nyquist sampling (130 nm pixel size) across the full width of a standard 25 mm CMOS camera (Hamamatsu Orca Flash 4.0 v3), yielding a total field of view of 266 microns. Emission filters were positioned in the focusing space immediately before the camera, and the entire detection assembly was built around a dovetail-based tube system, to ensure robust alignment and mechanical stability (**Figure 1a**). To facilitate precise axial positioning and accommodate different sample types, the entire detection assembly was mounted on a 50 mm travel focusing stage.

With the detection path establishing the necessary criteria for resolution, field of view, and optical alignment (e.g., beam height), we next designed the illumination system. In LSFM, the foci of the illumination and detection objectives must precisely overlap without mechanical interference, limiting the choice of compatible optics. To meet these requirements, we selected a 20x NA 0.6 long-working distance water immersion objective (Thorlabs TL20X-MPL). While Special Optics' equivalent objective offers a slightly higher NA, the Thorlabs objective allows for imaging on coverslips larger than 5 mm in diameter, improving ease of handling for end users. Guided by these constraints, we selected optical components capable of generating a theoretically diffraction-limited light-sheet using straightforward magnification calculations. To further improve illumination quality and reduce shadowing artifacts, we included a resonant multidirectional beam pivoting mechanism, ensuring even excitation throughout the sample[23].

The complete illumination system was designed for an input beam with a 2 mm diameter, which first passes through an achromatic doublet lens (f = 30 mm) followed by a second achromatic doublet (f = 80 mm), which expands and collimates it before reaching an achromatic cylindrical lens (f = 75 mm). This cylindrical lens focuses the beam in one direction, forming the initial light-sheet. The focal length of the cylindrical lens was chosen to be sufficiently large (≥ 60 mm) to allow adequate spacing between optical elements in the physical implementation of the system. The shaped beam is then directed onto a resonant galvanometer (**Supplementary Figure 1**). After reflection from a 45-degree tilted mirror, the beam is relayed through an achromatic doublet (f = 250 mm) before entering the back aperture of the illumination objective, where it is finally focused onto the sample. This optical arrangement ensures a well-defined, dynamically pivoted light-sheet that provides uniform illumination while mitigating shadowing effects.

In Silico Optimization of Altair-LSFM.

To ensure optimal illumination performance, we modeled the full illumination pathway of Altair-LSFM in Zemax OpticStudio (Ansys), systematically optimizing the relative placement of every optical element to achieve the desired focusing and collimation properties (**Figure 1b**). Each lens was iteratively adjusted to minimize aberrations and ensure precise beam shaping, enabling the formation of a well-defined light-sheet. The design was centered around a 488 nm illumination wavelength, with spatial axes defined following standard conventions: the Y-dimension represents the laser propagation direction, Z corresponds to the detection axis, and X is orthogonal to both. The final illumination system, depicted in Figure 1b, was optimized to generate a diffraction-limited light-sheet with a full-width-half-maximum (FWHM) of ~0.385 µm in Z, spanning the full 266 µm Field of view, as shown in **Figures 1c-d**.

Beyond idealized modeling, designing a physically realizable system requires an understanding of how fabrication tolerances affect optical performance. To assess system robustness, we performed a tolerance analysis, which quantifies sensitivity to mechanical perturbations. This analysis evaluates how small positional or angular deviations of optical elements—caused by manufacturing imperfections—impact key performance metrics such as light-sheet thickness and displacement from the ideal position, allowing us to systematically evaluate system stability (**Supplementary Figure 2a**). The perturbations analyzed were based on standard machining tolerances, typically ±0.005 inches, with higher-precision machining achievable at ±0.002 inches at increased cost. Given that Altair-LSFM was designed assuming the use of Polaris mounts, which incorporate DIN-7m6 ground dowel pins to aid with alignment, we considered the impact of angular misalignments caused by dowel pin positioning errors. In the worst-case scenario—where one dowel pin was offset by +0.005 inches and the other by -0.005 inches—the resulting angular deviation was ~1.45 degrees (**Supplementary Figure 2b**). To further assess system resilience, we conducted Monte Carlo simulations incorporating these perturbations, simulating a range of misalignment scenarios to quantify their effect on light-sheet performance. Our results showed that finer machining tolerances resulted in a worst-case performance closer to the nominal system, as visualized in **Supplementary Figure 2c**, which compares the nominal, best, and worst configurations. Notably, the analysis identified that angular offsets in the galvo mirror had the most significant impact on light-sheet quality, highlighting the importance of tighter machining tolerances for this component to maximize system stability and performance.

<u>Optomechanical Design of Altair-LSFM.</u>

Based on our simulation results, standard machining tolerances were deemed sufficient to construct a custom baseplate that ensures robust alignment, repeatable assembly, and a compact, plug-and-play design. Unlike cage- or rail-based systems, custom baseplates minimize variability by enforcing a fixed spatial relationship between optical components, enabling assembly by non-experts. Where possible, we eliminated all unnecessary degrees of freedom, restricting manual adjustments to only a few critical components. Specifically, we retained laser collimation (tip/tilt/axial position), galvo rotation, folding mirror alignment (tip/tilt), and objective positioning (tip/tilt/axial position).

To translate the numerically optimized positions of each optical element into a manufacturable design, the coordinates were imported into computer-aided design (CAD) software (Autodesk Inventor), ensuring precise positioning of all associated optomechanics. Where possible, Polaris optical posts and mounts were used to maintain consistency in mounting schemes and element heights. For components where a commercially available Polaris-compatible mount did not exist, such as the rotation mount (Thorlabs RSP1) for the cylindrical lens and the horizontal aperture (Thorlabs VA100), custom adapters were developed to seamlessly integrate them into the system. This approach allowed us to account for the offset between the optical element and its mechanical mount, ensuring that the baseplate was precisely machined with dowel pin locations and mounting holes (**Figure 2a, Supplementary Figure 3**). Additionally, the baseplate features four mounting holes at its corners, spaced such that it can be directly secured to an optical table or elevated using additional posts, allowing for easy adjustment of the illumination path height. This modular, precision-engineered design ensures both ease of use and long-term mechanical stability, enabling integration of Altair-LSFM into alternative experimental setups.

Beyond the illumination path, the full microscope system incorporates a variety of translational and custom mounting elements to facilitate precise sample positioning and stable imaging. A sample chamber was designed and 3D printed to match the working distances and clearances of the chosen illumination and detection objectives, offering two port configurations: one for traditional orthogonal imaging and another linear configuration that allows direct imaging of the light-sheet itself (**Figure 2b, Supplementary Figure 4**). Each port is equipped with two sets of O-rings, creating a liquid-proof seal around the objectives while still permitting smooth translation of the detection objective for focusing. Additionally, the snug fit of the O-rings naturally guide the user toward proper positioning of the illumination and detection objectives, decreasing the likelihood of alignment errors. The sample positioning assembly consists of three motorized translation stages (Applied Scientific Instrumentation), enabling precise positioning of the sample in x, y, and z. To enable rapid Z-stack acquisition, we designed an angled bracket ($\theta = 29.5$ degrees) for mounting a high-speed piezo (PiezoConcept HS1.100), which attaches directly to the sample positioning stages (**Figure 2c**). The sample is secured using a custom-designed sample holder for 5 mm glass coverslips, which features a clam-based mechanism-the coverslip is placed within a circular recess and secured in place by a screw-down clamp. Due to the angled sample scanning configuration, our collected image stacks must undergo a deskewing operation. All custom component designs, and deskewing software, are available for download at https://thedeanlab.github.io/altair.

Optoelectronic Design of Altair-LSFM.

In addition to simplifying the optomechanical design, we also streamlined the electronics and control architecture of Altair-LSFM to minimize complexity and improve system integration. To achieve this, we consolidated all control electronics into a single controller (TG16-BASIC, Applied Scientific Instrumentation), which manages the operation of all linear translation stages (X, Y, Z, and F), as well as the power supply for the resonant galvo and sample scanning piezo. This approach significantly reduces the number of auxiliary controllers and power supplies, simplifying the physical setup. Currently, all timing operations are performed using a 32-channel analog output device (PCIe-6738, National Instruments), which is responsible for generating the global trigger, controlling the camera's external trigger, modulating the laser through analog and digital signals, setting the piezo control voltage, and providing the DC voltage for adjusting the resonant galvo amplitude. An overview of the electronics used in the system, along with an associated wiring diagram, is provided in **Supplementary Figure 5** and **Supplementary Table 1**.

Alignment and Characterization of Altair-LSFM.

To evaluate optical performance, we first assembled and aligned the Altair-LSFM illumination system. The fiber-coupled laser source (Oxxius L4CC), which provides four excitation wavelengths (405 nm, 488 nm, 561 nm, and 638 nm), was introduced and collimated using tip/tilt mounts. The collimated beam was then directed onto the resonant galvo, which was rotated to reflect the beam downward toward the optical table. From there, the folding mirror was adjusted to guide the beam along the optical axis of the remaining components. Finally, the lateral position of the illumination objective was fine-tuned to ensure coaxial back-reflections, completing the alignment process. With the optical path aligned, we proceeded to validate system performance by characterizing the generated light-sheet by imaging it in transmission. As shown in **Figure 3a**, the light-sheet focus spans the full 266 µm field of view, closely matching our simulation results. Cross-sectional analysis of the full-width-at-half-maximum (FWHM) in the z-dimension, presented in **Figure 3b**, reveals a z-FWHM of ~0.415 µm. To assess the system's resolution, we imaged 100 nm fluorescent beads. The point spread function of a single isolated fluorescent bead is shown in **Figures 3c-e**, providing orthogonal perspectives of the bead's intensity distribution. The Gaussian-fitted distribution of FWHM measurements, performed on a population of fluorescent beads across a z-stack, is shown in **Figure 3f**. Prior to deconvolution, the average FWHM values measured across the bead population were 328 nm in x, 330 nm in y, and 464 nm in z. After deconvolution with PetaKit5D, these values improved to 235.5 nm (x), 233.5 nm (y), and 350.4 nm (z), achieving our desired resolution goals for sub-cellular imaging.

Sub-Cellular Imaging with Altair-LSFM

To demonstrate the imaging capabilities of Altair-LSFM in a biological context, we prepared and imaged mouse embryonic fibroblasts (MEFs) cells stained for multiple subcellular structures. The staining protocol enabled visualization of the nucleus (DAPI, 405 nm, cyan), microtubules (488 nm, gray), actin filaments (561 nm, gold), and the Golgi apparatus (638 nm, magenta), corresponding to the excitation channels of our system. Deconvolved maximum intensity projections of the labeled cells is shown in **Figure 4a** and **Figure 4f**, with each individual corresponding fluorescence channel presented in **Figures 4b-e** and **Figures 4g-j**. The imaging results reveal fine nucleolar features within the nucleus, with perinuclear Golgi structures distinctly visible. Additionally, stress fibers are clearly resolved in the actin channel, and individual microtubules appear well-defined, highlighting the system's ability to capture cytoskeletal structures with high resolution. These results confirm that Altair-LSFM provides the sub-cellular resolution, optical sectioning, and multi-color imaging performance necessary for quantitative biological imaging applications.

Discussion:

In this work, we demonstrated the viability of a baseplate-based approach for the disseminating a high-performance light-sheet microscope that is both accessible and easy to assemble by non-experts. By combining optical simulations, precision-machined component design, and experimental validation, we developed Altair-LSFM, a system that delivers sub-cellular resolution imaging with minimal alignment requirements. Characterization using fluorescent beads confirmed that Altair-LSFM achieves a resolution of 328, 330, and 464 nm before deconvolution, which improves to 235.5, 233.5, and 350.4 nm after deconvolution, in X, Y, and Z, respectively. These values are on par with LLSM, confirming that our approach achieves state-of-the-art performance but in a streamlined, cost-effective, and reproducible format. A complete parts list, and estimated cost, are provided in **Supplementary Tables 2 and 3**, respectively, offering a transparent roadmap for users looking to adopt and build the system.

Building on this successful prototype, future efforts will focus on expanding both imaging capabilities and user experience. One natural evolution of this approach is the development of more advanced light-sheet microscope designs, such as Axially Swept Light-Sheet Microscopy[12,24] and Oblique Plane Microscopy[13,25], which offer additional flexibility for imaging a broader range of sample types. Another avenue for improvement is the optimization of Altair-LSFM for cleared-tissue imaging, further extending its applicability into tissue contexts. Additionally, we aim to eliminate the need for an external analog output device, consolidating all triggering and waveform generation within a single unified controller, which will reduce hardware dependencies and enhance system efficiency.

Another important consideration is the long-term scalability and routine maintenance of Altair-LSFM in a variety of lab environments. While our initial prototype has shown reliability, multi-site benchmarking and community feedback will be pivotal to ensure consistent, reproducible performance across different setups. Future enhancements—such as self-alignment routines—could further boost imaging quality and throughput. To accelerate widespread adoption, we have thoroughly documented the entire assembly process in our GitHub repository[26], which is also provided as a **Supplementary Document**, and are holding on-site workshops aimed at equipping researchers with the hands-on skills needed to assemble and operate a Altair-LSFM system. By fostering open collaboration and continuous software-hardware integration, we envision Altair-LSFM evolving into a robust, ever-improving platform, well-suited to meet future research challenges in high-resolution, volumetric imaging.

A persistent challenge in advanced microscopy is the lengthy interval—from instrument conceptualization to commercialization—often spans close to a decade. By offering modular, high-performance microscope designs that can be assembled and operated by non-experts, we hope to drastically shorten this timeline. Integrating these systems with navigate[27], our open-source microscope control software, will further democratize intelligent imaging workflows and broaden the reach of cutting-edge instrumentation. With high-NA imaging, reduced mechanical and optical complexity, and lower cost, Altair-LSFM stands poised to accelerate LSFM adoption, delivering a powerful yet accessible solution for researchers immediately seeking access to high-resolution, cutting-edge, volumetric imaging.

Acknowledgements
The authors would like to thank Calvin Jones and Dr. Sophia Theodossiou (Boise State University) for their assistance in designing and printing the custom sample chamber, and Melissa Glidewell for her initial evaluation of optical tolerances. This work was supported by the National Institutes of Health (U54 CA268072 and RM1 GM145399).

Conflicts of Interest
K.M.D. is a co-inventor on a patent covering ASLM and a founder of Discovery Imaging Systems, LLC. K.M.D. also has consultancy agreements with 3i, Inc (Denver, CO, USA).

Author Contributions
J.H., formal analysis, investigation, methodology, validation, visualization, and writing. S.G., resources, visualization, and writing. K.M.D. funding acquisition, investigation, methodology, project administration, software, resources, supervision, visualization, and writing.

Materials and Methods
Acquisition and Simulation Computer. All microscope control and optical simulations were performed on a Colfax SX6300 workstation, configured to handle high-speed data acquisition and processing. It is equipped with dual Intel Xeon Silver 4215R processors (8 cores, 16 threads, 3.2 GHz), 256 GB of DDR4 3200 MHz ECC RAM, a 7.68 TB Samsung PM9A3 NVMe SSD for high-speed data acquisition, a 20 TB Seagate Exos X20 HDD for long-term data storage, a PNY NVIDIA T1000 4 GB GPU, and an Intel X710-T2L dual-port 10GbE.

Cell Culture and Fixation. Mouse embryonic fibroblast (MEFs) cells were cultured in Dulbecco's Modified Eagle's Medium (DMEM, Gibco) supplemented with 10% fetal bovine serum (FBS, Gibco) and 100 µg/mL penicillin-streptomycin. The cells were maintained at 37°C in a humidified incubator with 5% CO_2 and cultured in a 12-well plate on 5 mm cover slips, pre-rinsed with 70% ethanol. After reaching ~50% confluency, cells were rinsed with 1x Phosphate-Buffered Saline (PBS) and incubated in pre-heated 37°C PEM buffer [80 mM PIPES, 5 mM EGTA, 2 mM $MgCl_2$, (pH: 6.8)], supplemented with 0.3% Triton-X and 0.125% glutaraldehyde (GA) for 30 s. Next, cells were fixed in a PEM buffer supplemented with 2% paraformaldehyde (PFA) for 15m at 37 °C and washed three times with 1x PBS, 2 min each.

Immunofluorescence. All incubations were performed at room temperature with constant agitation unless otherwise specified. Cells were quenched in 5 mM glycine for 10 min. Blocking was conducted for 1 h in 3% bovine serum albumin (BSA) + 0.01% Triton-X in 1x PBS. Indirect immunofluorescence was applied for microtubules and Golgi apparatus visualization. Specifically, cells were incubated with primary antibodies: Anti-α-Tubulin (Sigma-Aldrich, #T9026, 1:250) and GOLGA/GM130 (Proteintech, #11308-1-AP, 1:500) in staining buffer [1% BSA + 0.01% Triton-X in 1x PBS] overnight at 4°C, following by three washes with PBST [0.01% Triton-X in 1x PBS], 2 min each. Cells were then incubated in staining buffer with secondary antibodies: Donkey Anti-Mouse CF488A (Biotium, #20014-1, 1:500) and Donkey anti-Rabbit Alexa Fluor 647 (Thermo Fisher Scientific, #A-31573, 1:500) for 1 h, and three washes with PBST were repeated. Actin filaments were stained with Phalloidin Conjugate CF568 (Biotium, #00044, 1:50) in 1x PBS for 1h. Finally, cells were incubated in DAPI nuclear dye (Thermo Fisher Scientific, #62248, 300 nM) in 1x PBS for 10 min. Samples were stored at 4°C in 1x PBS with 0.02% sodium azide (NaN_3) until imaging.

Preparation of Fluorescent Bead Samples. A 5 mm glass coverslip was placed inside a petri dish, and approximately 100 µL of (3-Aminopropyl)triethoxysilane (APTS) at a concentration of 5 mM was applied to its surface. The APTS was incubated for 10–30 min to promote bead adhesion, after which the coverslip was lightly washed three times with deionized water. Fluorescent beads (Fluoresbrite YG Microspheres 0.10 µm, Polyscience, Inc) were diluted to

the desired concentration (typically 10^{-3} or 10^{-4} for a normal distribution, 10^{-6} for a sparse distribution) and applied to the treated coverslip, where they were incubated for 2–20 min, with longer incubation times increasing bead density. Finally, the coverslip was lightly washed with DI water to remove unbound beads before imaging.

Custom Machining and Fabrication. All metal components were machined from 6061-T6x aluminum by Protolabs or Xometry, adhering to standard machining tolerances of ±0.005 inches. The sample chamber was 3D printed using a Formlabs Form 3B resin printer with standard black resin. CAD files for all custom parts are provided as a supplementary file, with up-to-date versions available on GitHub.

References

1 Huisken, J., Swoger, J., Del Bene, F., Wittbrodt, J. & Stelzer, E. H. Optical sectioning deep inside live embryos by selective plane illumination microscopy. *Science* **305**, 1007-1009 (2004). https://doi.org/10.1126/science.1100035

2 Voie, A. H., Burns, D. H. & Spelman, F. A. Orthogonal-plane fluorescence optical sectioning: three-dimensional imaging of macroscopic biological specimens. *J Microsc* **170**, 229-236 (1993). https://doi.org/10.1111/j.1365-2818.1993.tb03346.x

3 Lange, M. *et al.* A multimodal zebrafish developmental atlas reveals the state-transition dynamics of late-vertebrate pluripotent axial progenitors. *Cell* **187**, 6742-6759 e6717 (2024). https://doi.org/10.1016/j.cell.2024.09.047

4 Gao, R. *et al.* Cortical column and whole-brain imaging with molecular contrast and nanoscale resolution. *Science* **363** (2019). https://doi.org/10.1126/science.aau8302

5 Ahrens, M. B., Orger, M. B., Robson, D. N., Li, J. M. & Keller, P. J. Whole-brain functional imaging at cellular resolution using light-sheet microscopy. *Nat Methods* **10**, 413-420 (2013). https://doi.org/10.1038/nmeth.2434

6 Planchon, T. A. *et al.* Rapid three-dimensional isotropic imaging of living cells using Bessel beam plane illumination. *Nat Methods* **8**, 417-423 (2011). https://doi.org/10.1038/nmeth.1586

7 Gao, L., Shao, L., Chen, B. C. & Betzig, E. 3D live fluorescence imaging of cellular dynamics using Bessel beam plane illumination microscopy. *Nat Protoc* **9**, 1083-1101 (2014). https://doi.org/10.1038/nprot.2014.087

8 Chen, B. C. *et al.* Lattice light-sheet microscopy: imaging molecules to embryos at high spatiotemporal resolution. *Science* **346**, 1257998 (2014). https://doi.org/10.1126/science.1257998

9 Chang, B.-J. *et al.* Universal light-sheet generation with field synthesis. *Nature Methods* **16**, 235-238 (2019). https://doi.org/10.1038/s41592-019-0327-9

10 Chang, B.-J., Dean, K. M. & Fiolka, R. Systematic and quantitative comparison of lattice and Gaussian light-sheets. *Optics Express* **28** (2020). https://doi.org/10.1364/oe.400164

11 Wu, Y. *et al.* Spatially isotropic four-dimensional imaging with dual-view plane illumination microscopy. *Nat Biotechnol* **31**, 1032-1038 (2013). https://doi.org/10.1038/nbt.2713

12 Dean, Kevin M., Roudot, P., Welf, Erik S., Danuser, G. & Fiolka, R. Deconvolution-free Subcellular Imaging with Axially Swept Light Sheet Microscopy. *Biophysical Journal* **108**, 2807-2815 (2015). https://doi.org/10.1016/j.bpj.2015.05.013

13 Sapoznik, E. *et al.* A versatile oblique plane microscope for large-scale and high-resolution imaging of subcellular dynamics. *eLife* **9** (2020). https://doi.org/10.7554/eLife.57681

14 Diederich, B. *et al.* A versatile and customizable low-cost 3D-printed open standard for microscopic imaging. *Nat Commun* **11**, 5979 (2020). https://doi.org/10.1038/s41467-020-19447-9

15 Chen, Y. *et al.* Low-cost and scalable projected light-sheet microscopy for the high-resolution imaging of cleared tissue and living samples. *Nat Biomed Eng* **8**, 1109-1123 (2024). https://doi.org/10.1038/s41551-024-01249-9

16 Jahr, W., Schmid, B., Weber, M. & Huisken, J. eduSPIM: Light Sheet Microscopy in the Museum. *PLoS One* **11**, e0161402 (2016). https://doi.org/10.1371/journal.pone.0161402

17 Girstmair, J., Moon, H., Brillard, C., Haase, R. & Tomancak, P. Time to Upgrade: A New OpenSPIM Guide to Build and Operate Advanced OpenSPIM Configurations. *Adv Biol (Weinh)* **6**, e2101182 (2022). https://doi.org/10.1002/adbi.202101182

18 Pitrone, P. G. *et al.* OpenSPIM: an open-access light-sheet microscopy platform. *Nat Methods* **10**, 598-599 (2013). https://doi.org/10.1038/nmeth.2507

19 Gualda, E. J. *et al.* OpenSpinMicroscopy: an open-source integrated microscopy platform. *Nat Methods* **10**, 599-600 (2013). https://doi.org/10.1038/nmeth.2508

20 Vladimirov, N. *et al.* Benchtop mesoSPIM: a next-generation open-source light-sheet microscope for cleared samples. *Nat Commun* **15**, 2679 (2024). https://doi.org/10.1038/s41467-024-46770-2

21 Voigt, F. F. *et al.* The mesoSPIM initiative: open-source light-sheet microscopes for imaging cleared tissue. *Nat Methods* **16**, 1105-1108 (2019). https://doi.org/10.1038/s41592-019-0554-0

22 Kumar, A. *et al.* Dual-view plane illumination microscopy for rapid and spatially isotropic imaging. *Nature Protocols* **9**, 2555-2573 (2014). https://doi.org/10.1038/nprot.2014.172

23 Huisken, J. & Stainier, D. Y. Even fluorescence excitation by multidirectional selective plane illumination microscopy (mSPIM). *Opt Lett* **32**, 2608-2610 (2007). https://doi.org/10.1364/ol.32.002608

24 Dean, K. M. *et al.* Isotropic imaging across spatial scales with axially swept light-sheet microscopy. *Nature Protocols* (2022). https://doi.org/10.1038/s41596-022-00706-6

25 Chang, B.-J. *et al.* Real-time multi-angle projection imaging of biological dynamics. *Nature Methods* **18**, 829-834 (2021). https://doi.org/10.1038/s41592-021-01175-7

26 Dean, K. M., Haug, J. & Gałecki, S. *altair*, <https://thedeanlab.github.io/altair/> (2025).

27 Marin, Z. *et al.* Navigate: an open-source platform for smart light-sheet microscopy. *Nat Methods* (2024). https://doi.org/10.1038/s41592-024-02413-4

28 Otomo, K. *et al.* descSPIM: an affordable and easy-to-build light-sheet microscope optimized for tissue clearing techniques. *Nat Commun* **15**, 4941 (2024). https://doi.org/10.1038/s41467-024-49131-1

29 Liu, Y., Rollins, A. M. & Jenkins, M. W. CompassLSM: axially swept light-sheet microscopy made simple. *Biomed Opt Express* **12**, 6571-6589 (2021). https://doi.org/10.1364/BOE.440292

Figures

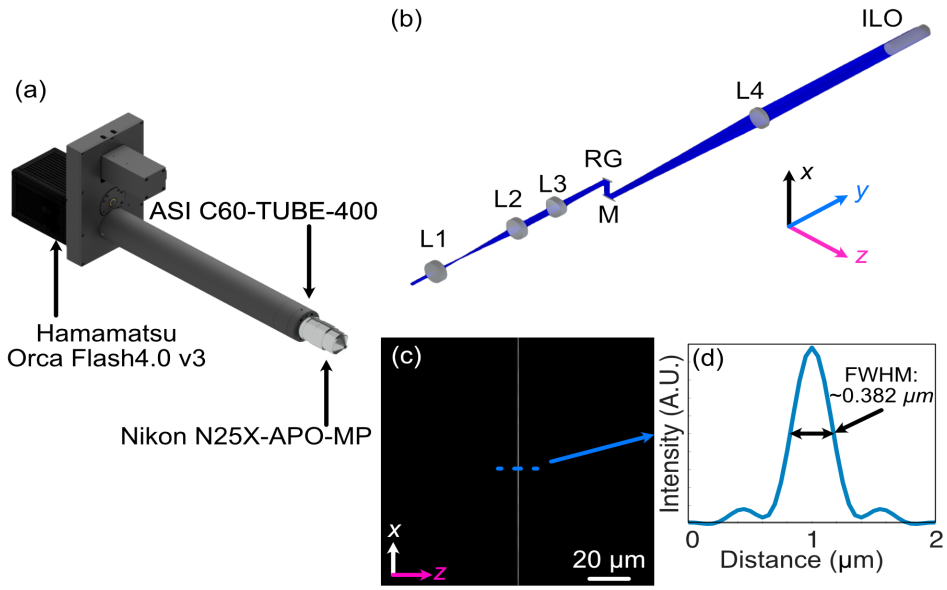

Figure 1 - **(a)** Rendering of the detection arm elements. **(b)** Zemax Opticstudio layout and beam path of optimized illumination arm, where L1 is an f = 30 achromatic doublet, L2 is an f = 80 mm achromatic doublet, L3 is the f = 75 mm achromatic cylindrical doublet, and ILO is our TL20X-MPL illumination objective. **(c)** The simulated light-sheet beam profile in the xz plane at the focus of the illumination objective. **(d)** The cross-sectional profile through the center of the light-sheet beam profile in (c), where the FWHM of the light-sheet was found to be 0.382 µm.

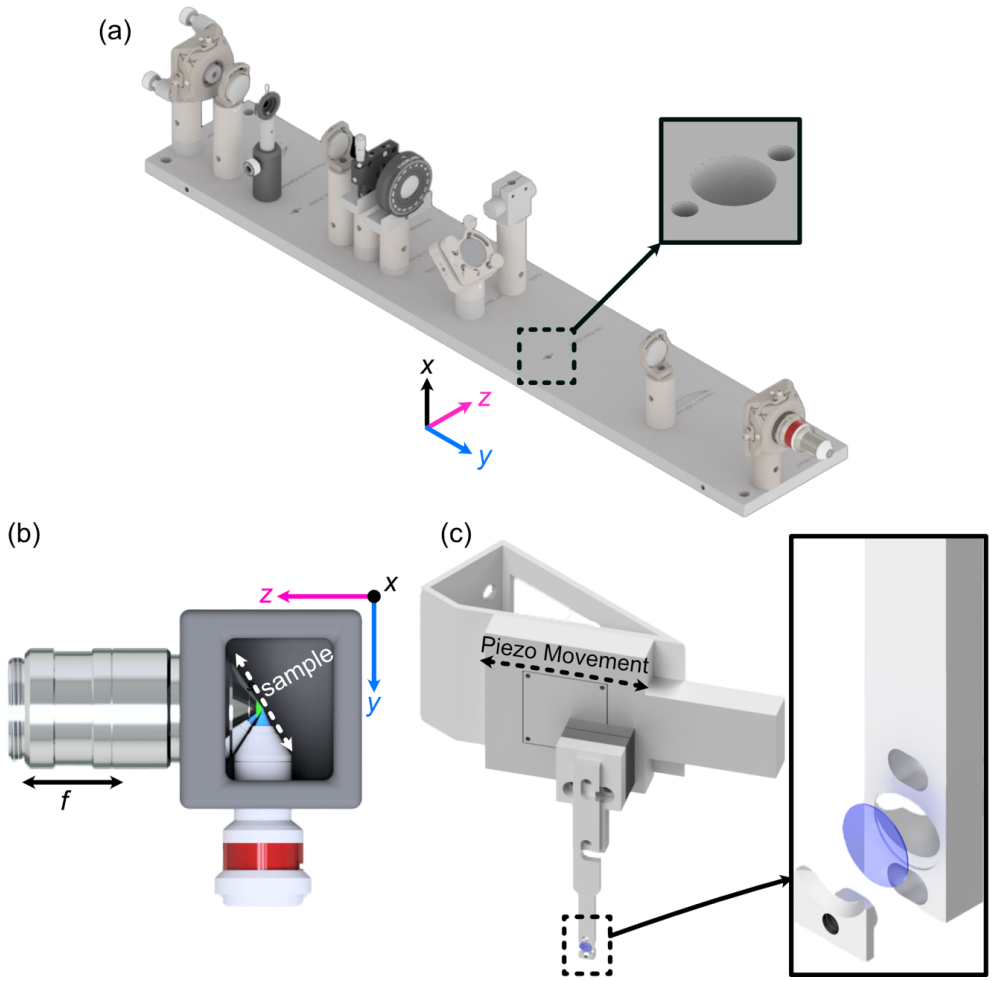

Figure 2 - (a) Rendering of the completed illumination arm baseplate, with an inset showing the dowel pin holes compatible with the Polaris mounting line from Thorlabs. **(b)** Overhead view of the imaging configuration of our system, where our detection objective and illumination objectives are placed orthogonal to each other and the sample is scanned diagonally in the space between them in the axial direction shown by the white dashed line. **(c)** Rendering of our sample mounting and translation system. Here, a piezo motor is mounted onto an angled adapter to allow precise translation over the diagonal region between the objectives. Our custom 5 mm coverslip sample holder is also featured, where the inset shows an exploded assembly of the holder.

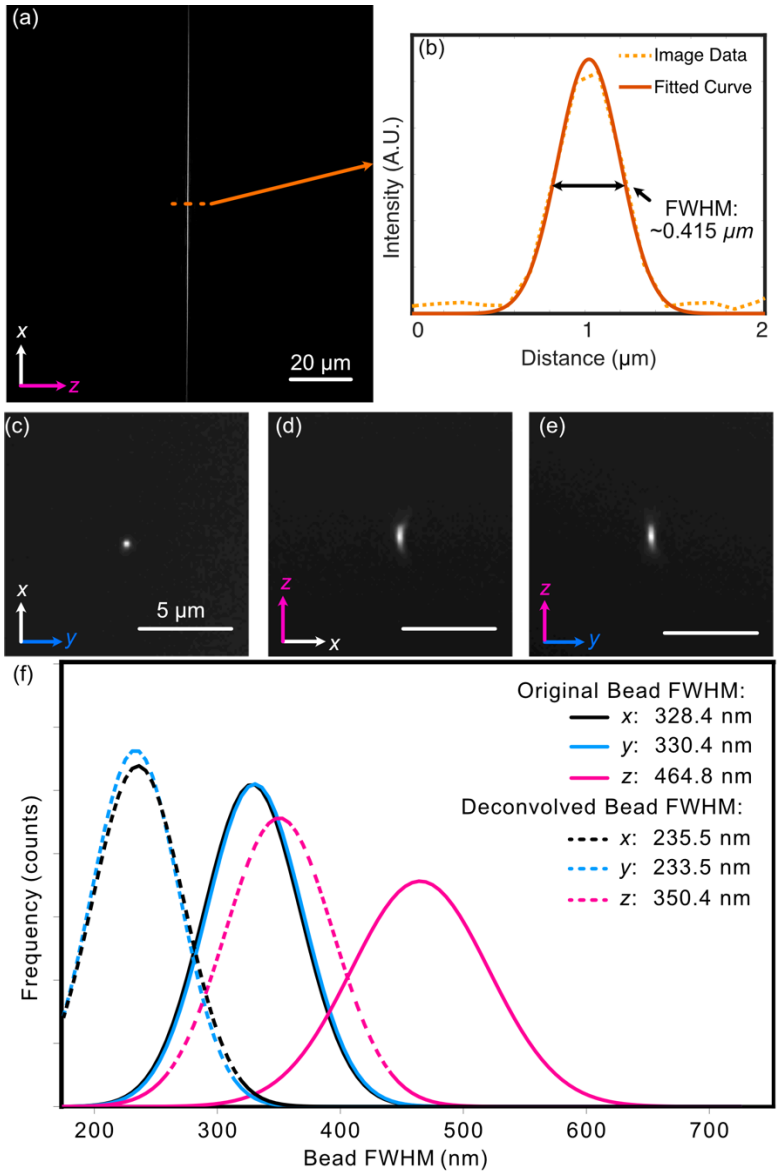

Figure 3 - **(a)** Experimental light-sheet beam profile at the focus **(b)** The center cross-section profile of (a), showing both raw data and a fitted curve with a FWHM of ~0.415 µm. **(c-e)** Max intensity projections for an isolated 100 nm fluorescent bead in each of the 3 orthogonal planes **(f)** Gaussian-fitted distribution of the FWHM of beads imaged in a z-stack in each dimension both before (solid) and after (dashed) deconvolution.

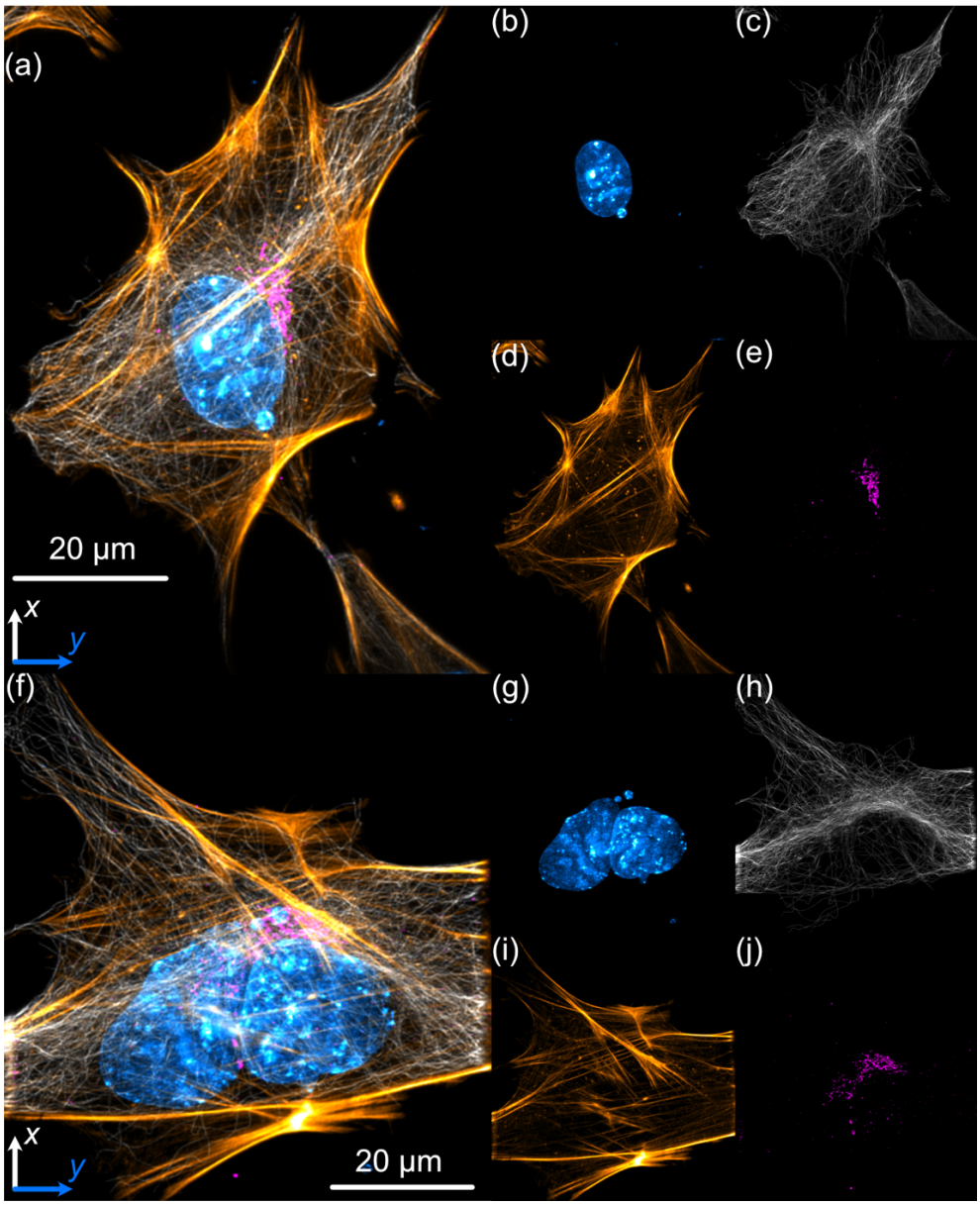

Figure 4 – Lateral maximum intensity projections of mouse embryonic fibroblasts (MEFs) fluorescently labeled with nuclei (cyan), tubulin (gray), actin (gold), and the Golgi apparatus (magenta). (a) Maximum intensity projection of the full z-stack in the xy plane. (b–e) Individual channels corresponding to (a): (b) nuclei, (c) microtubules, (d) actin, and (e) Golgi apparatus. (f) Maximum intensity projection of a second z-stack in the xy plane. (g–j) Individual channels corresponding to (f): (g) DAPI, (h) microtubules, (i) actin, and (j) Golgi apparatus. Nuclei were labeled with DAPI, actin filaments with phalloidin, and both microtubules and the Golgi apparatus were stained using indirect immunofluorescence.

417 **Tables**

418

Microscope	Illumination Optics	Detection Optics	Design
OpenSPIM[18]	Olympus UMPLFLN 10XW NA 0.3 (Water)	UMPLFLN 20XW NA 0.5 (Water)	Rail Carrier
X-OpenSPIM[17]	Nikon CFI Plan Fluor 10X NA 0.3 (Water)	Nikon CFI Apochromat NIR 40X W NA 0.8 (Water)	Rail Carrier
EduSPIM[16]	Zeiss LSFM 5X NA 0.1 (Air)	Zeiss LD Epiplan 5X NA 0.13 (Air)	Cage System
OpenSPIN[19]	Nikon CFI Plan Fluor 4X NA 0.13 (Air) Nikon Plan Fluor 10X NA 0.3 (Air)	Nikon CFI Plan Fluor 4X NA 0.13 (Air) Nikon CFI75 LWD 16X NA 0.8 (Water)	Rail Carrier
UC2[14]	Generic 4X NA 0.14 (Air)	Generic 4X NA 0.14 (Air) Generic 10X NA 0.3 (Air)	3D Printed Components
pLSM[15]	Mitutoyo Plan Apo 10X NA 0.28 (Air)	Mitutoyo Plan Apo 10X NA 0.28 (Air) ASI 54-10-12 16.67X NA 0.4 (Multi-Immersion)	Cage System
descSPIM[28]	500- and 150-mm cylindrical lenses (Air)	Thorlabs TL2X-SAP 2X NA 0.1 (Air)	Cage System
mesoSPIM[21]	Nikon 50 mm f/1.4 G (Air)	Olympus MVPLAPO 1X NA 0.15 (Air)	Rail Carrier
BT-mesoSPIM[20]	Nikon 50 mm f/1.4 G (Air)	Variable. Magnification 2-20X, NA 0.1-0.28 (Air)	Cage System
diSPIM[11]	Nikon CFI Apochromat NIR 40X W NA 0.8 (Water)	Nikon CFI Apochromat NIR 40X W NA 0.8 (Water)	Dovetail Tube System
CompassLSM[29]	Olympus XLFLUOR 4x NA 0.28 (Air/Water)	Olympus MVX PLAPO 1x NA 0.25 (Air) Olympus MVX PLAPO 2XC NA 0.5 (Air) Olympus UPlanFL 4x NA 0.13 (Air) Nikon CFI Plan Apo 10XC NA 0.5 (Water)	Rail Carrier
Lattice Light-Sheet Microscopy (LLSM)[8]	Special Optics 54-10-7 28.6X NA 0.67 (Water)	Nikon CFI75 Apochromat 25XC NA 1.1 (Water)	Free Space Optics
Altair-LSFM	Thorlabs TL20X-MPL 20X NA 0.6 (Water)	Nikon CFI75 Apochromat 25XC NA 1.1 (Water)	Custom Baseplate & Dovetail Tube System

Table 1. LSFM variants and their associated illumination and detection optics. The table lists the type of microscope, the illumination and detection optics-including NA where available and immersion type in parentheses-as well as the overall design architecture (e.g., rail carrier, cage system, etc.).

Supplementary Figures

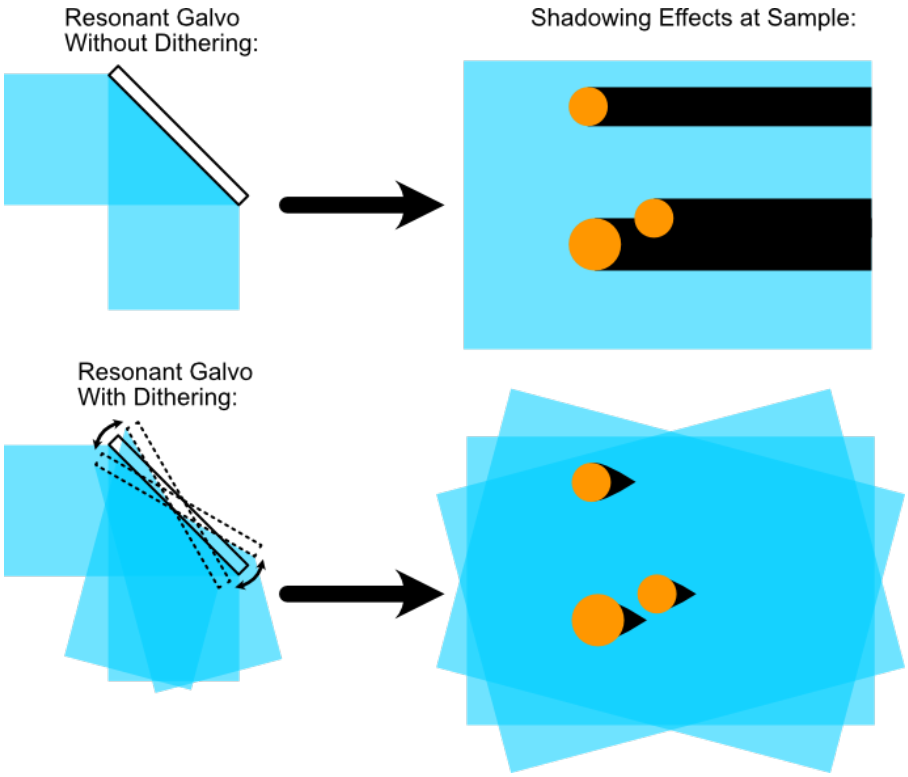

Supplementary Figure 1 – Function of the resonant galvo unit, where without dithering, objects in a sample can cast shadows. Incorporation of dithering at a high speed over the image acquisition time effectively averages the effects of these shadows out of the final image.

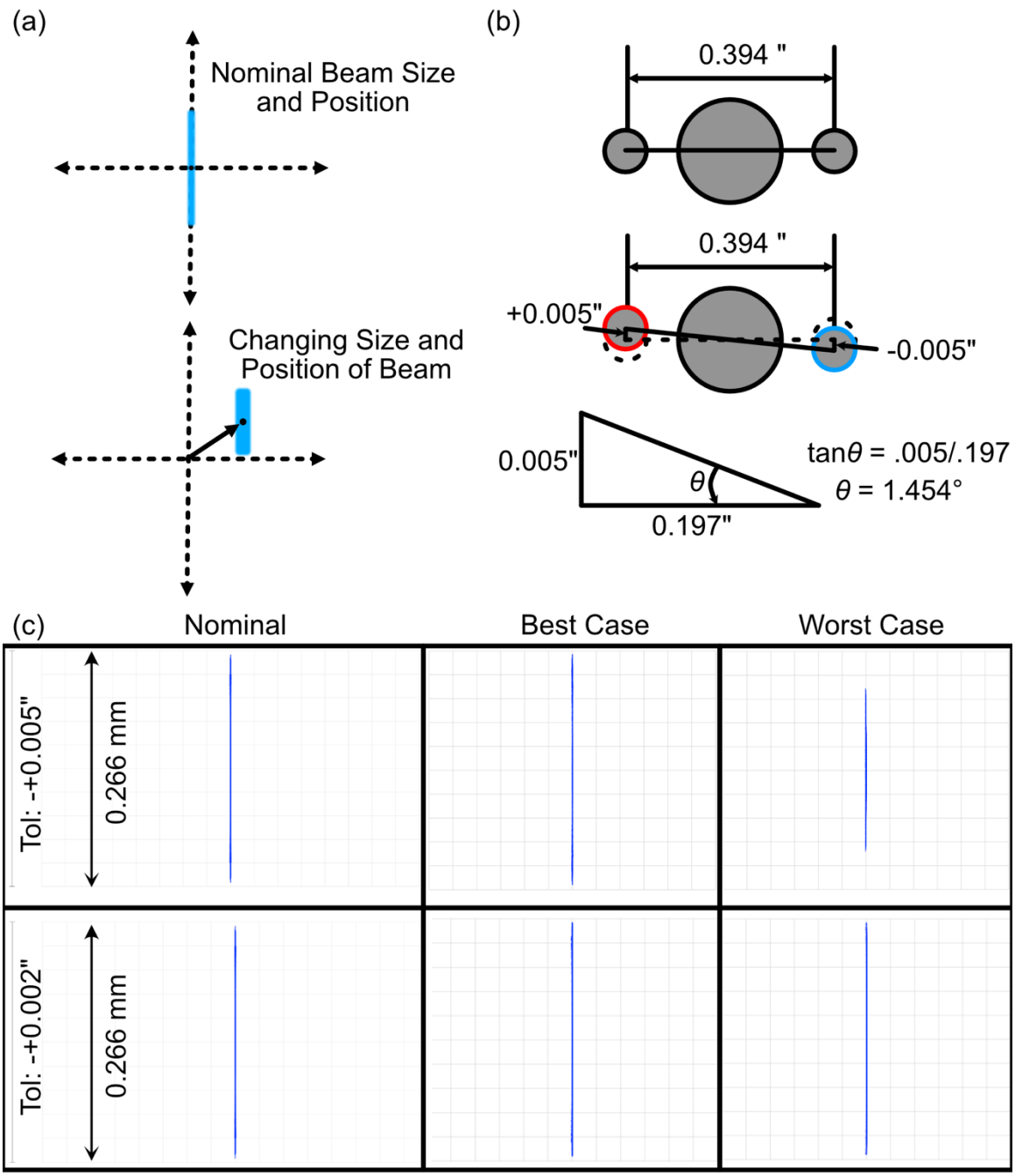

Supplementary Figure 2 - **(a)** Depiction of the merit function criteria used in our tolerance analysis, where we observed how the beam profile in the perturbed instances changes in both size and position. **(b)** Schematic of the Polaris dowel pin mounting configuration when considering machining tolerances, where in a worst-case scenario the angle offset would be 1.454 degrees. **(c)** Nominal, best case, and worst-case beam profiles in *xz* for both coarse (+-0.005", top row) and fine (+-0.002", bottom row) machining tolerances.

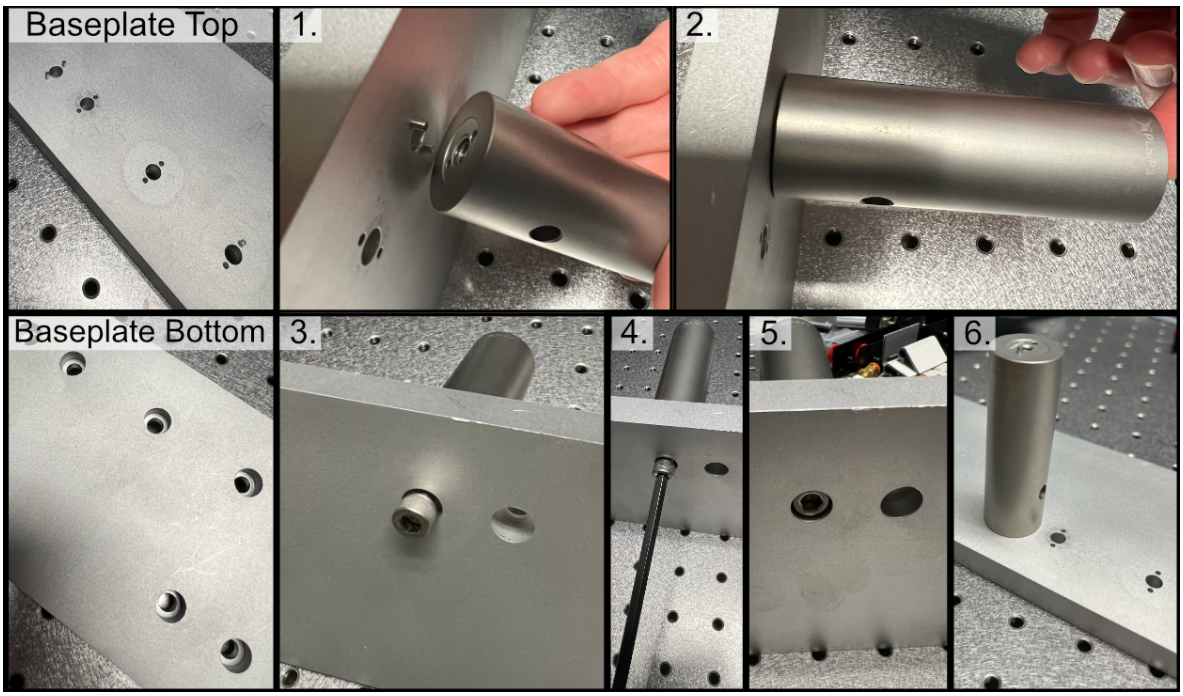

Supplementary Figure 3 – Process of affixing a post to the baseplate, where one first places the post onto dowel pins inserted into the corresponding holes and then fixes the post to the baseplate with a screw.

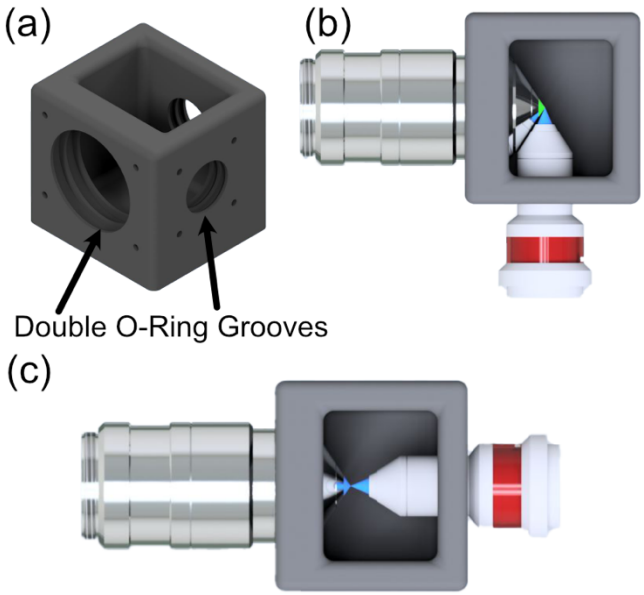

Supplementary Figure 4 - **(a)** CAD rendering of our custom sample chamber, featuring three possible objective ports, each with two sets of O-rings to ensure a liquid-proof seal. **(b)** Top-down rendering of the traditional imaging configuration for the system, where the illumination and detection objectives are placed orthogonal to one another. **(c)** The second imaging configuration of the system used to image the beam itself, where the illumination objective is place directly in front of the detection objective.

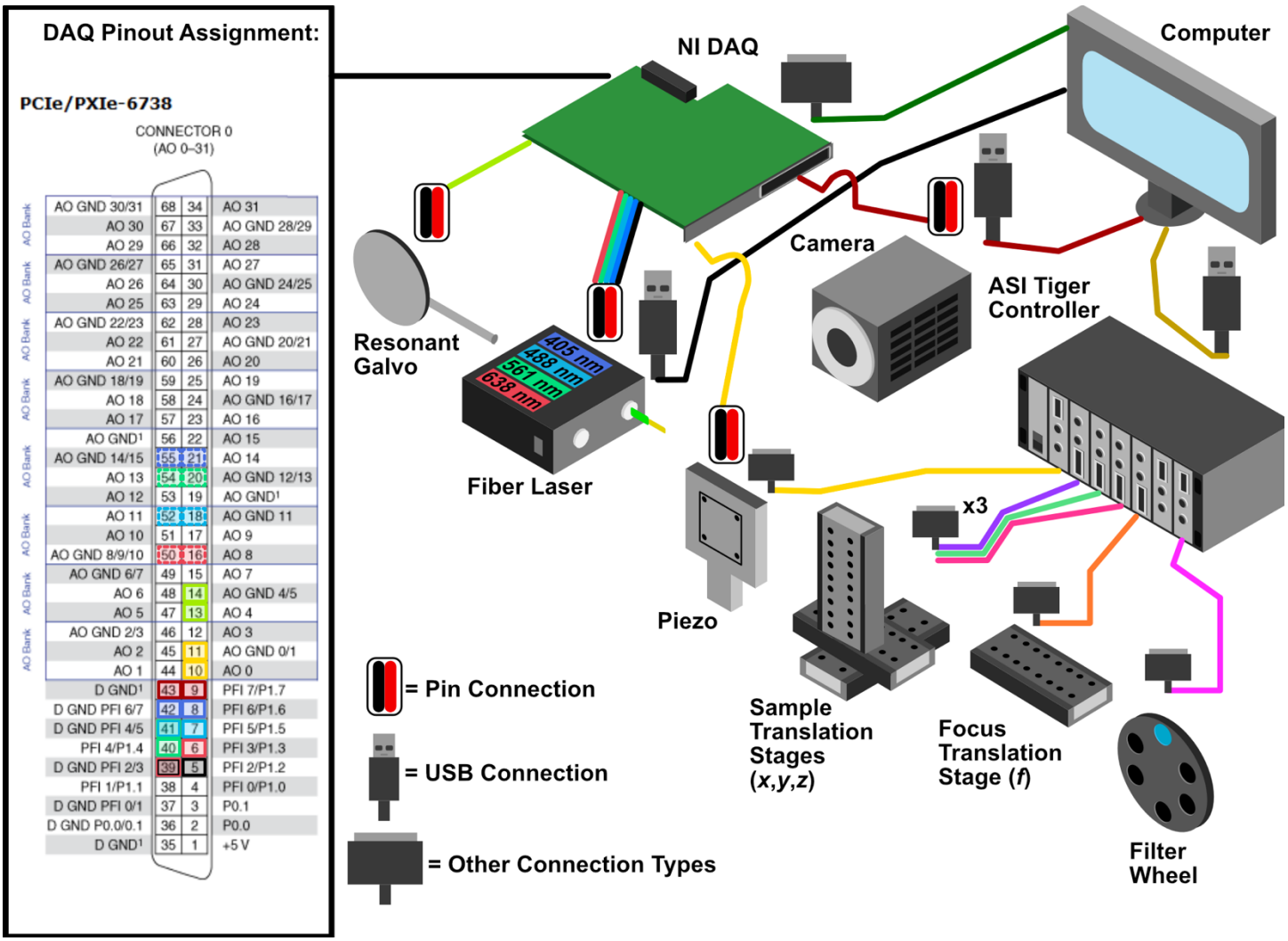

Supplementary Figure 5 – General wiring diagram of the system showing all of the optoelectrical and optomechanical components used, and an inset showing how these components are wired into the NI DAQ.

Supplementary Tables

Component	Analog/Digital?	Ground Pin	Active Pin
Resonant Galvo	Analog	14	13
Piezo Motor	Analog	11	10
Camera	Digital	43	9
Fiber Laser (FL) Output Shutter	Digital	39	5
FL λ = 405 nm AO Port	Analog	55	21
FL λ = 405 nm IO Port	Digital	42	8
FL λ = 488 nm AO Port	Analog	18	52
FL λ = 488 nm IO Port	Digital	41	7
FL λ = 561 nm AO Port	Analog	20	54
FL λ = 561 nm IO Port	Digital	41	40
FL λ = 638 nm AO Port	Analog	50	16
FL λ = 638 nm IO Port	Digital	39	6

Supplementary Table S1. Electrical pinouts used on National Instruments PCIe-6738 data acquisition card. All analog and digital connections were made using a National Instruments SCB-68A shielded terminal block.

Name	Manufacturer	Description	Qty	Approximate Cost Per
Shared Equipment				
TG16-BASIC	ASI	Tiger Controller – 16 Bay System	1	$6,350
PCIe-6738	NI	Data Acquisition Card	1	$2,200
SCB-68A	NI	Noise Rejecting Terminal Block	1	$500
SHC68-68-A2	NI	Test Cable Assembly	1	$250
784-736-02R	TMC	36x60x18” Performance Series Optical Top	1	$6,275
14UD-42X-24	TMC	Ultradamp Vibration Isolation with Casters	1	$9,300
SX6300	Colfax International	Colfax SX6300 Workstation	1	$6,800
Detection Path				
LS-100-AMCCH	ASI	100 mm Linear Focusing Stage, 16 TPI	1	$2,250
TGDCM2	ASI	2-Axis Stage Control Card	1	$1,050
C60-EXT-15	ASI	15 mm Tube Extension	1	$75
RAO-0051	ASI	M32x0.75 Threaded Sleeve	1	$150
FW-0002-8	ASI	8-Position Filter Wheel	1	$3,500
FW-C-MNT-K1	ASI	Filter Wheel to MIM Adapter Kit	1	$400
C60-TUBE-400	ASI	400 mm Achromatic Tube Lens	1	$875
TGFW	ASI	Filter Wheel Control Card	1	$1,150
C13440-20CU	Hamamatsu	ORCA Flash4.0 V3	1	$16,500
OH-CAMRA-1007	Hamamatsu	Firebird CamLink Board	1	$2,000
N25X-APO-MP	Thorlabs	Nikon 25x NA 1.1 Detection Objective	1	$33,810
445/20-25nm	Semrock	Brightline Bandpass filter	1	$375

529/24nm	Semrock	Brightline Bandpass filter	2	$375
605/15-25nm	Semrock	Brightline Bandpass filter	1	$375
676/29-25nm	Semrock	Brightline Bandpass filter	1	$375
Sample Positioning				
LS-5012	ASI	Breadboard Adapter	1	$160
LS-5013	ASI	Right Angle Bracket	1	$250
DV-6010-C	ASI	Dovetail Mount Pair	1	$230
LS-50-AMCLLS	ASI	50 mm Linear Stage with Stainless Steel Slide	1	$2,425
LS-100-AMERL	ASI	100 mm Linear Stage, 16 TPI, Extended, Right	1	$3,100
LS-50-AMELL	ASI	50 mm Linear Stage	1	$2,250
TGADEPT	ASI	Piezo Control Card	1	$1,500
HS1.100	PiezoConcept	Piezo Concept 100 Micron Piezo Stage	1	$4,100
ADAPTHS1BB	PiezoConcept	Adapter Plate for PiezoConcept HS1	1	$120
Angle Bracket Adapter	Xometry	Angle adapter for mounting piezo at an angle	1	$592.58
Illumination Path				
L4CC	Oxxius	Multicolor Laser Source	1	25,000
P3-405B-FC-1	Thorlabs	Fiber Cable Single Mode FC/APC	1	$120
CFC11A-A	Thorlabs	Fiber Collimator	1	$370
Polaris-K1XY	Thorlabs	Kinematic Mount for Fiber Laser Collimator	1	$1375
AC254-030-A-ML	Thorlabs	Achromatic Lens f=30mm (L1)	1	$125
AC254-080-A-ML	Thorlabs	Achromatic Lens f=80mm (L2)	1	$115
ACY254-075-A	Thorlabs	Achromatic Cylindrical Lens f=75mm (L3)	1	$445
AC254-250-A-ML	Thorlabs	Achromatic Lens f=250mm (L4)	1	$90
PF10-03-P01	Thorlabs	1” Protected Silver Mirror	1	$55
TL20X-MPL	Thorlabs	Illumination Objective	1	$4820
VA100CP	Thorlabs	Rectangular Aperture	1	$315
IDA12	Thorlabs	Circular Aperture Iris	1	$60
Polaris-P150	Thorlabs	1” Diameter Polaris Mounting Post, 1.5” Length	1	$45
Polaris-P2	Thorlabs	1” Diameter Polaris Mounting Post, 2” Length	1	$45
Polaris-P3	Thorlabs	1” Diameter Polaris Mounting Posts, 3” Length	3	$45
Polaris-P075*	Thorlabs	1” Diameter Polaris Mounting Post, 0.75” Length	1	$45
Polaris-P225*	Thorlabs	1” Diameter Polaris Mounting Post, 2.25” Length	1	$45
Polaris-P250*	Thorlabs	1” Diameter Polaris Mounting Post, 2.5” Length	2	$45
Polaris-MA45	Thorlabs	Polaris 45 Degree Adapter for Mirror Mount	1	$50
Polaris-B1S	Thorlabs	Polaris Flexure-Closed Lens Mount	3	$110
Polaris-1XY	Thorlabs	Polaris XY Translation Mount for Illumination Objective	1	$1020
Polaris-K1S4	Thorlabs	Polaris 1” Mirror Mount	1	$185

SM1A12	Thorlabs	Thread Adapter for Illumination Objective into Polaris-1XY	1	$25
6SC04KA040-01Y	Novanta	1-Axis 4 kHz Resonant Galvo and Servo	1	$3,700
Galvo Holder	Protolabs	Holder for Galvo	1	$400
TGPOW-12-3	ASI	Galvo Low Noise Power Supply +12V 3A	1	$950
RSP1 Adapter	Xometry	Custom Adapter for Thorlabs RSP1 to Polaris Posts	1	$80
VA100CP Adapter	Xometry	Custom Adapter for Thorlabs VA100CP to Polaris Posts	1	$80
CP02 Adapter	Xometry	Custom Adapter for Thorlabs CP02 to Polaris Posts	1	$80
Illumination Path Baseplate	Xometry	Baseplate for Illumination Path	1	$1000

Supplementary Table S2. Detailed equipment list. Prices are approximate and subject to change-often unpredictably due to economically self-defeating trade wars. *Indicates that the part was custom ordered from Thorlabs.

Group	**Approximate Cost**
Illumination Path	$41,195
Sample Positioning	$14,727
Detection Path	$63,635
Shared Equipment	$31,675
Total:	$151,232

Supplementary Table S3. Approximate Cost